Article:
Hinks, T, Carr, H, Gharibi, H et al. (1 more author) (2015) Visualisation of urban airborne laser scanning data with occlusion images. ISPRS Journal of Photogrammetry and Remote Sensing, 104. pp. 77-87. ISSN 0924-2716

https://doi.org/10.1016/j.isprsjprs.2015.01.014

Visualisation of Urban Airborne Laser Scanning Data with Occlusion Images

Tommy Hinks[a], Hamish Carr[b], Hamid Gharibi[a], Debra F. Laefer[a,*]

[a] *Urban Modelling Group, School of Civil, Structural and Environmental Engineering, University College Dublin, Ireland*
[b] *Visualization and Virtual Reality Group, School of Computing, University of Leeds, United Kingdom*

Abstract

Airborne Laser Scanning (ALS) was introduced to provide rapid, high resolution scans of landforms for computational processing. More recently, ALS has been adapted for scanning urban areas. The greater complexity of urban scenes, necessitates the development of novel methods to exploit urban ALS to best advantage. This paper presents occlusion images: a novel technique that exploits the geometric complexity of the urban environment to improve visualisation of small details for better feature recognition. The algorithm is based on an inversion of traditional occlusion techniques.

Keywords: Airborne Laser Scanning, LiDAR, Ambient Occlusion, Urban Modelling, Elevation Image

1. Introduction

In recent decades Airborne Laser Scanning (ALS) has emerged as an effective tool for acquiring accurate point data over large areas. As a form of Light Detection And Ranging (LiDAR), ALS uses an aircraft-mounted laser that reflects pulses of light from the ground and then computes the spatial positions from which pulses are reflected. The resulting point data can then

*Corresponding Author: School of Civil, Structural and Environmental Engineering, University College Dublin, Newstead, Belfield, Dublin 4, Ireland. Tel: +353 1 716 3226

Email addresses: tommy.hinks@gmail.com (Tommy Hinks), h.carr@leeds.ac.uk (Hamish Carr), hamid.gharibi@ucdconnect.ie (Hamid Gharibi), debra.laefer@ucd.ie (Debra F. Laefer)

be used in fields such as hydrology (Hollaus et al., 2005), forestry (Hollaus et al., 2006; Yu et al., 2011), disaster management (Laefer and Pradhan, 2006; Corbane et al., 2011) and glaciology (Geist et al., 2003; Arnold et al., 2006).

ALS has also been applied to urban modelling, in which the goal is to create models of buildings across an entire city either for visual reconstruction or for computational modelling. Urban ALS has thus been used to identify buildings and other permanent man-made structures (Dorninger and Pfeifer, 2008; Tournaire et al., 2010; Huang et al., 2013) as well as road networks (Clode and Rottensteiner, 2007; Elberink, 2010), power lines (Melzer and Briese, 2004), and urban vegetation (Rutzinger et al., 2008).

In order to minimize time and cost, several highly automated building extraction methods have been introduced, in particular for loosely spaced and fairly uniform suburban buildings (Rottensteiner et al., 2005; Matikainen et al., 2007; Awrangjeb et al., 2010). For dense urban centres, however, where buildings abut each other and a greater variety of buildings occur, extraction methods still rely heavily on human intervention, and, therefore, on visualisation of the point data. Additionally, even highly automated building extraction methods require some form of visualisation to evaluate the success rates and to allow for manual correction of the results.

While orthophotos and other resources, such as ground plans, are sometimes useful in building extraction (e.g. (Haala et al., 1998)), they cannot be used to visualise errors that happen in the acquisition process. Moreover, such resources are often outdated making them difficult to use in many scenarios. As such, there appears to be an increasing trend to use methods that are data driven. Common examples of these types of methods used to visualise ALS point data and to prepare them for segmentation include the following: (1) elevation images, (2) intensity images, and (3) colour images. Elevation images are created by mapping ALS points to pixels and assigning grey-scale values proportional to the highest elevation in the mapped points appearing in each pixel. This approach enables visualising ALS data as grey-scale images, which has the effect of emphasizing the building outlines. In contrast, in intensity images the pixel values are assigned from the intensities of the return laser pulses recorded for each point. Finally, colour images can be directly generated from the ALS data, as some ALS systems (e.g. FLI-MAP400) are equipped with a line scan camera fitted to the laser scanner, which is used to generate a type of colour values for each laser return. However, for dense urban areas, none of these visualization pro-

cesses are individually robust due to geometric complexities, small features, closely abutting buildings, intermingled vegetation, and the presence of large volumes of traffic within the urban context.

To address these existing deficits an alternative method is proposed to visualise urban ALS point data. This method is entitled occlusion images and employs the differential visibility of walls, roofs, and small building features when sampled from multiple directions. In particular, the similarity between this problem and an existing technique in computer graphics - ambient occlusion (Zhukov et al., 1998) is exploited (and basically inverted) to better visually articulate architecturally significant features.

2. Urban ALS Acquisition and Visualisation

2.1. Acquisition

For the purposes of this paper, it is assumed that high-quality ALS data have been acquired for an urban centre using redundant overlapping strips to cover the area of interest. For details see (Hinks et al., 2009); as well as the survey papers by (Baltsavias, 1999a,b,c,d) for an overview of the ALS acquisition process. In order to understand the use of occlusion, however, some key characteristics of how the data is acquired are introduced (Figure 1).

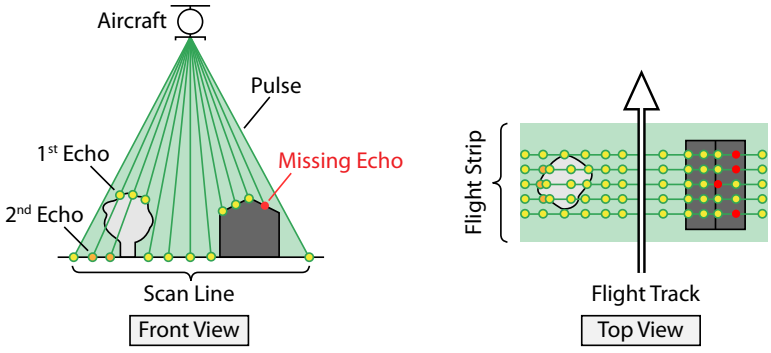

Figure 1: *Left*: Pulses are emitted at regular, angular intervals in scan lines. For each pulse a number of echoes may be detected. If no echoes are detected, no points are recorded for that particular pulse. Consecutive scan lines are parallel and fairly regularly spaced in the flight track direction.

The aircraft typically flies above the area of interest in straight flight tracks. Points recorded during a flight track are collectively referred to as

a flight strip (Figure 1). In this paper, it is assumed that points are acquired in roughly parallel scan lines. Other scan patterns exist, as described in (Baltsavias, 1999b). As the aircraft moves forward, laser pulses are emitted sideways by rotating a mirror that deflects the laser before it exits the aircraft (Latypov, 2005). Each scan line is acquired by emitting pulses at regular angular intervals in the direction perpendicular to the flight direction, as shown in Figure 1. Typically, the scan rate is largely compared to the speed of the aircraft and, therefore, the aircraft is often considered to be stationary during the acquisition of a single scan line. An additional complication is that some pulses may not return a detectable signal, but this can be remedied by interpolating additional points (Hofle, 2007).

The aircraft typically flies above the area of interest in multiple flight tracks. While it is technically feasible to have curved flight tracks, the best quality data generally results from a straight and level flight, as illustrated in Figure 2. Related work (Hinks et al., 2009) has shown that urban details can be captured more consistently using heavily overlapped flight strips, low aircraft altitude, and flight tracks that are oriented in two diagonal directions. Based on this study, an ideal flight path would include flight tracks offset from each other at a distance of 1/3 of the total scan width (Figure 2, left). In other words, the overlap between flight strips is about 67%, plus a slight increase to avoid lacuna in the data.

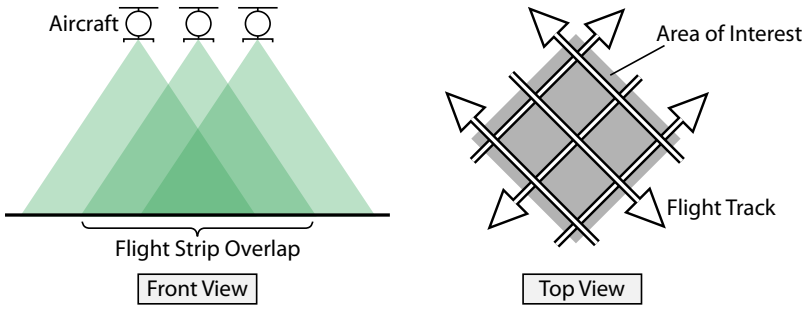

Figure 2: As described in (Hinks et al., 2009), high quality point data for urban areas can be obtained from heavily overlapped flight strips (left) in two diagonal directions (right).

2.2. Visualisation

Once the ALS data have been acquired, it is necessary to visualise them. Visualisation is also a common processing step for the building extraction

process. As explained in Section 1, an overhead view is constructed either directly from the return pulse intensities or by generating a grey-scale image from the point elevations in the ALS data. The latter will be referred to herein as an elevation image. Sometimes, when the ALS system is able to record colour values for the points (e.g. the ALS system that has been used in this project), a colour image can also be created to visualise the ALS data.

Elevation images for visualising urban centres have two characteristic problems: non-uniform building geometries and loss of architectural details. In a typical urban centre, there is a wide range of building sizes, heights, and shapes. Since a human is relatively insensitive, only 10 to 20 (out of the 256 grey-scale levels) can be consistently discerned. Thus, if an image contains centimeter-scale measurements for buildings that range from 10 m to 100 m in height, an elevation image either appears saturated, in which case tall buildings are in effect truncated or very coarsely represented. In such cases the geometric details captured by the ALS scan are lost in the visualisation.

In contrast, colour images are easier to interpret, but colour represents surface properties rather than geometry. Since pavement and road materials are very similar to those of buildings, detecting building footprints for densely packed buildings surrounded by streets and sidewalks can be extremely challenging by colour alone. Moreover, urban centres are also populated by transient objects such as vehicles and pedestrians, which draw attention due to their contrast against the background. As a result, neither elevation nor colour images are ideally suited for visualisation of urban centres.

3. Test Data

For this study, an area of approximately 1 km^2 in the city centre of Dublin, Ireland was selected. Data acquisition involved a winter 2007 flight, based on the patterning proposed by (Hinks et al., 2009), which included flight strips that overlapped by 67%. Specifications of the airborne LiDAR system and the collected data are summarized in Table 1.

4. Occlusion Images

The previous section identified the difficulties in visualising building footprints from elevation and colour images. Alternatively, what is desired is an image derived directly from the ALS data, in which transient objects are not represented, while permanent geometric boundaries are emphasized (as

Table 1: Specifications of the airborne LiDAR system and the collected data

Items	Values
LiDAR system	FLI-MAP 2 System
Scan Angle (°)	60 (30 on each side)
Scanning Rate ($scanline/s$)	150
Pulses per Second	1000 (maximum of 4 echos per pulse)
Angular Spacing of Pulses (rad)	0.001
Quoted Horizontal Accuracy (cm)	8
Quoted Vertical Accuracy (cm)	5
Aircraft Altitude (m)	350 - 400
Number of Flight Strips	40
Number of points ($million$)	225
Horizontal Point Density (pts/m^2)	25

opposed to identifying a single maximum elevation level). Such an image can be achieved by exploiting the fact that the visibility of a vertical or horizontal surface from the sky is consistent over time and largely independent of elevation.

In particular, because the scanned geometry is sampled from multiple directions in overlapping flight strips, visibility varies across the image. Patterns caused by the scanned geometry can be visualised. The resulting images are referred to herein as occlusion images. This idea, of considering visibility from multiple directions, has already been studied in a different context - that of ambient occlusion (Zhukov et al., 1998).

Figure 3 shows an example of an occlusion image in the context of some common image types used to visualise ALS data, as discussed previously in Section 2.2. Two types of spectral images are shown in the top row: a colour image (Figure 3a) generated from colour values recorded for ALS points and an intensity image generated from the return pulse intensity values (Figure 3b). As shown, neither is well-suited for geometric analysis, since image complexity makes geometric boundary determination difficult. This is largely because colour is a visual property, while the task of identifying buildings is fundamentally geometric in nature. In the elevation image (Figure 3c) large structures are visible, but smaller structures, such as roof details and built-up courtyards, are suppressed by limitations in contrast caused by the presence of tall buildings. The occlusion image (Figure 3d) does not suffer from the contrast issues of the elevation image. In Figure 3d, the building

boundaries are clearly visible, while buses and trees are suppressed, and saturation problems due to elevation ranges do not occur. Large structures are clearly visible, as well as small-scale details on roofs and spaces in-between buildings. The suppression of transient objects and foliage will be discussed in further detail in Section 5.4.

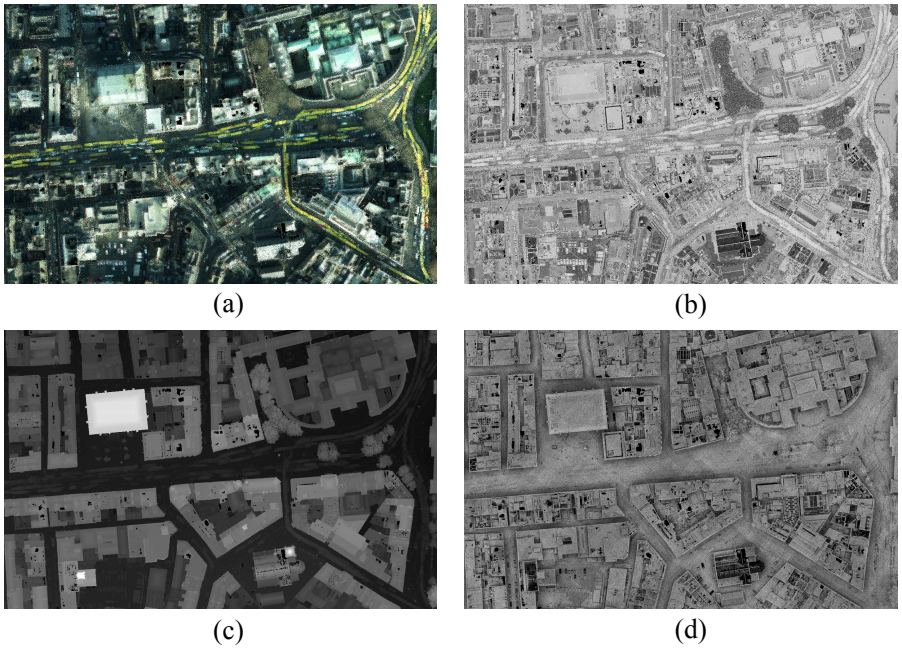

Figure 3: Comparison between the proposed occlusion image and other common image types used for ALS data visualisation: (a) colour image generated from colour values associated with ALS points, (b) intensity image constructed from the return laser pulse intensities, (c) elevation image, and (d) occlusion image. Pixel dimensions in global coordinates are $\Delta x = \Delta y = 0.25\ m$ in all images.

4.1. Ambient Occlusion

Computer graphics seeks to produce realistic images by simulating how light interacts with surfaces. Ideally rendering simulates individual photons (e.g. (Jensen, 2009)), but this is computationally expensive, and cheap approximations are, therefore, preferred. In particular, several studies have shown that shadowing effects play an important role for human perception of shapes and geometric details (Stewart and Langer, 1997; Langer and Buelthoff, 2000).

One method for approximating shadows is known as ambient occlusion (Zhukov et al., 1998). This method relies on the observation that surface points that are more exposed to the sky receive more illumination than points that are occluded. Exposure, or visibility, to the sky is typically computed at surface points by casting rays in a number of directions and testing whether any other objects occlude the ray, before it reaches the sky. As shown in Figure 4, rays are traced from points A and B towards the sky. Because point A is close to the building, sky visibility is more limited than at point B. Thus, point A is more shadowed than point B.

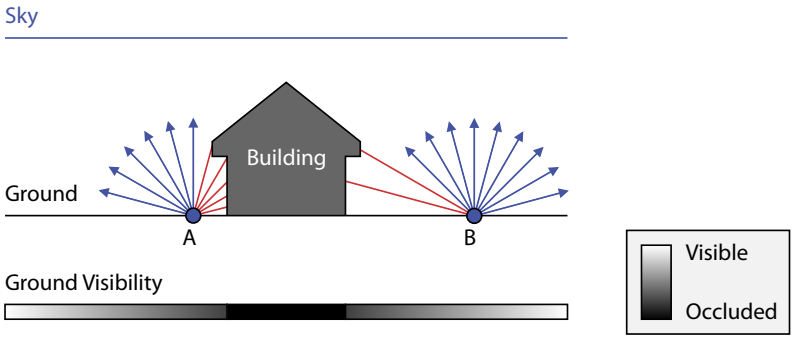

Figure 4: In ambient occlusion, sky visibility is computed by tracing rays from surface points towards the sky in a fixed number of directions.

4.2. Ambient Occlusion to Occlusion Images

In general, in a complex scene such as an urban centre, sky visibility decreases (i.e. occlusion increases) near objects (i.e. buildings). Moreover, ALS data are acquired by casting rays from the sky towards the ground: the inverse of ambient occlusion. Therefore, constructing an occlusion image by reversing the ALS rays and accumulating them in pixels of the image is possible. Implicitly, this integrates the information over the multiple flight strips, with the effect that transient objects such as vehicles, pedestrians, or cranes are less strongly represented than permanent objects such as buildings. Moreover, because the walls of buildings are visible throughout their vertical height, while ground locations are strongly occluded by the surrounding buildings, building footprints show up clearly in the resulting images, as do geometric details of complex building structures.

In practice, ALS data sets are often delivered as a point cloud - i.e. a collection of points $\{p_i\}$ in three dimensions. Yet, they are in actuality each

geo-registered to the aircraft's position so that the correct global coordinates for each point can be determined. As a result, the location in sky where each scan ray was emitted can either be extracted from the data delivered or inferred from the time stamp associated with each point. Thus, each sample is not only a point on the surface scanned but also an attestation that a particular surface point was visible from a specific sky location at a unique point in time.

An additional twist is that a given scan ray may strike several surfaces due to laser beam divergence and, therefore, return multiple echoes, represented by multiple points in the data sharing a common scan ray. These situations are addressed by dividing one unit of visibility between all points sharing a common scan ray. Since this can only be resolved by treating all of these points at once, the points p_i are sorted according to their time-stamp, and all points sharing a common scan ray q_j are processed at once. Each ray q_j then contributes a total of one unit of visibility to the occlusion image that is divided evenly among all its points. Hence, the visibility contribution of each point, v_p, is defined as follows:

$$v_p = \frac{1}{N_p} \tag{1}$$

where N_p is the total number of points sharing the ray q_i. The occlusion image is, then, constructed by defining an image whose pixels represent squares on the ground, with all pixels initialised to zero (i.e. no sky visibility or equivalently complete occlusion). Visibility for pixels is determined by accumulating visibility contributions of mapped points. However, a pixel cannot receive more than one unit of visibility from a single sky location. Thus, pixel visibility, v_{pix}, is computed as:

$$v_{pix} = \min\left(1, \sum v_p\right) \tag{2}$$

where $\sum v_p$ is the total amount of visibility contributions of the mapped points appearing in the pixel. More specifically, visibility is accumulated under the constraint that a unique sky location only contributes a single unit of visibility to a pixel, as shown in Figure 5. Visibility distributions of four scan rays are illustrated in Figure 5. The leftmost ray has three echo points (a, b, and c), while the second and third points (b and c) are both mapped to pixel A. These two points (b and c) each contribute 1/3 visibility, generating a total of 2/3 visibility in pixel A. The first echo point

(a) of this ray maps to a different pixel (B), which receives a contribution of 1/3 pixel visibility. The second ray from the left has only one point (d), which contributes exactly one unit of visibility to pixel C. The two rightmost scan rays, which are hitting the wall of a building, each has one echo point. Thus, each of these two points (e and f) contributes one unit of visibility and both are mapped to the same pixel D. However, based on Equation 2 a pixel cannot receive more than one unit of visibility from any single sky location. Therefore, the visibility of pixel D is always equal to one.

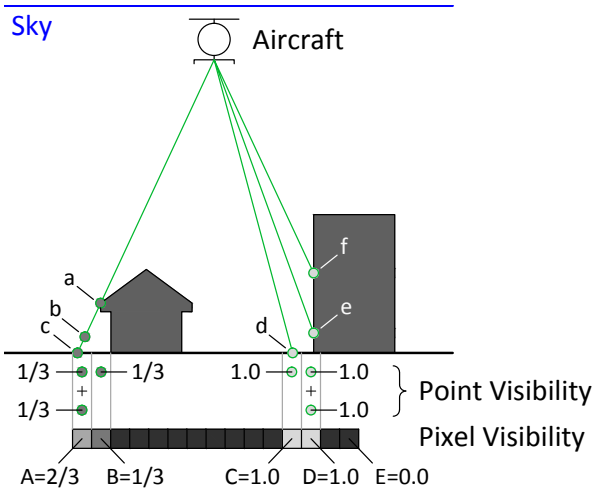

Figure 5: Each scan ray is considered to be one unit of visibility evenly distributed across its component echo points. Final pixel visibility is equal to the sum of the visibility of the mapped points appearing in the pixel, but with the constraint that a pixel cannot receive more than one unit of visibility from a single sky location.

When visibility from two or more sky locations is accumulated, interesting occlusion patterns start to emerge. In the end, the image is normalized to the unit interval $[0, 1]$ and visualised as a grey-scale image. Figure 6 illustrates the pixel-wise addition of visibility from the two sky locations P_0 and P_1. Note how the building roof is visible from both sky locations, whereas regions on the ground near the building are mostly visible from only one of the two locations. Note also how the rightmost part of the scene is not visible from P_0 (and by symmetry the leftmost part is invisible from P_1). Because of this, the edges of the scene receive visibility from only one sky location. This stresses the importance of flight strip overlap for useful visibility patterns to emerge, since the ground near the edges is not recognised as having clear

views of the sky, even though they have it; overlap by additional flight strips would have rectified this.

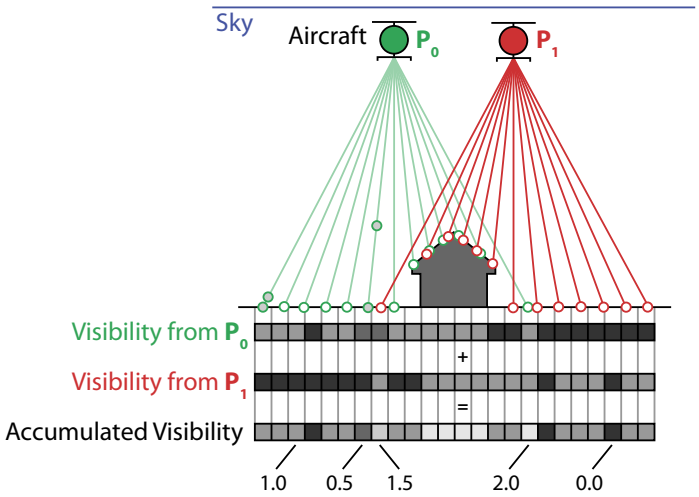

Figure 6: Visibility accumulation from multiple sky locations is defined as the pixel-wise addition of visibility from individual sky locations.

In the examples above, each scan line has been considered to be acquired from a unique sky location. Even though this is notionally true, in the sense that the aircraft is considered to be stationary during the acquisition of a single scan line, it is possible to extend the concept of unique sky locations to be more flexible. The following section describes how to extend the concept of sky location sampling to enable smoothing of irregularities caused by small variations in aircraft orientation.

4.3. Flight Path Sampling

An additional issue rises in practice - namely that some regions of the data will have more overlapping than others. This occurs primarily near the edges of flight strips due to small changes in aircraft position and orientation caused by factors such as strong winds and navigational inaccuracies. Such variations in aircraft orientation cause irregularities in point sampling and, by extension, visibility mapping. However, small variations in aircraft orientation tend to cancel out over time. Thus, by considering points acquired during time-intervals (as opposed to instantaneous scan lines) as representing visibility from a single sky location, it becomes possible to avoid some artefacts related to irregular point sampling.

A single flight path point describes instantaneous information about the aircraft position. In order to describe aircraft motion over time, it is necessary to explicitly derive some form of connectivity between flight path points. A hierarchical structure is used to describe connectivity for varying lengths of time as shown in Figure 7. Based on this structure, different levels of the flight path hierarchy can be treated as unique sky locations during the creation of occlusion images. At the finest level, interpolated aircraft positions for every scan line are treated as unique sky locations. Moving up the hierarchy, the next level is to treat points acquired in each flight path segment (representing one second of scanning), as being sampled from unique aircraft positions. Similarly, entire flight tracks can be treated as unique sky locations, where the scanning time represented by each flight track may vary. The following example demonstrates how this works in practice.

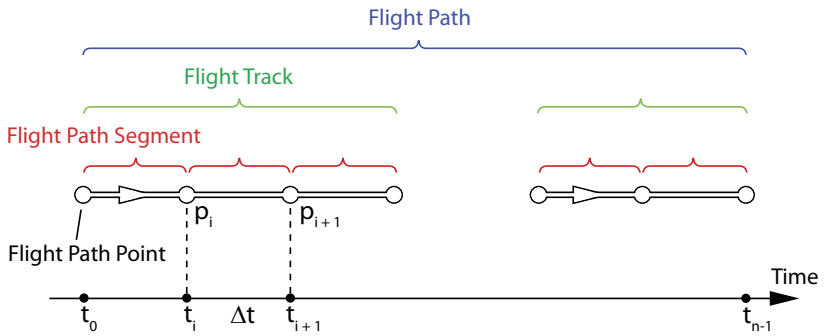

Figure 7: A hierarchical model describing the motion of an aircraft over time including the following elements: interpolated flight path points for each scan line (black); flight path segments (red) consisting of two connected flight path points; flight tracks (green) consisting of connected segments; and the flight path (blue) comprised of all flight tracks.

Based on the hierarchy shown in Figure 7, different occlusion images can be created using the distinctive levels of the flight path. Figure 8 shows how the output of the technique varies depending upon the portion of the flight path hierarchy that is used, with brighter pixels indicating higher visibility. The cyan coloured markings show notional sky locations used in the visibility mapping step. In Figure 8a, the interpolated aircraft position for individual scan lines were considered to be unique sky locations. Small variations in aircraft pitch over time caused parts of the flight strip to be over- or under-sampled, whereby some pixels receive visibility contributions from multiple sky locations that are very closely spaced, leading to bright streaks

in the across-track direction. In ambient occlusion terms this is equivalent to casting multiple rays in nearly identical directions, which is not indicative of overall sky visibility.

In comparison, Figure 8b shows the effect of using one second time segments as sky locations. Many of the bright streaks are eliminated, but artefacts are still present in some areas due to aircraft orientation being unstable for longer than one second. However, visibility mapping is clearly more uniform, as illustrated by the lower amount of contrast in this image.

Finally, in Figure 8c, the entire flight strip was considered to be acquired from the same sky location. Any variations in aircraft orientations are irrelevant in this case, since only a single sky location is considered. This approach is superior when points are assumed to be acquired only in the across-track direction. However, many ALS systems, including the one used to obtain the data in this work, acquire both forward and backward looking scan lines, as well as across-track ones. Hence, considering sky locations in the along-track direction becomes important, since forward and backward visibility vary significantly for different aircraft positions in a flight strip. The effects of flight path sampling will be demonstrated in more detail in the next section.

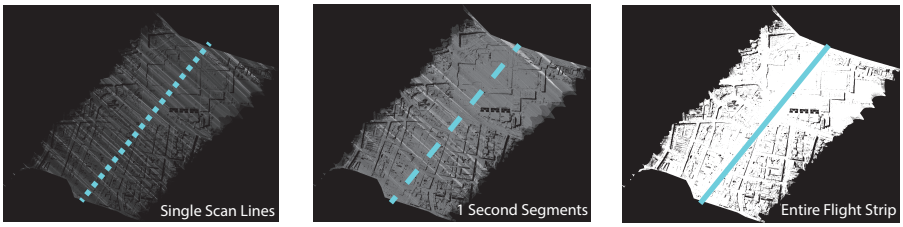

Figure 8: Occlusion images generated with different definitions of unique sky locations: (a) scan lines, (b) one second segments and (c) entire flight strip. Pixel dimensions are $\Delta x = \Delta y = 0.50\ m$ in all images.

4.4. Visibility Accumulation

To generate interesting occlusion patterns, multiple overlapping flight strips are required. This will ensure that ALS point mapping to the same pixel are potentially acquired from different sky locations, thus confirming visibility in several directions. In ambient occlusion terms, the amount of flight strip overlap corresponds closely to the number of visibility rays being

cast from each surface point. However, unlike in the ambient occlusion technique, in occlusion images, the surfaces points are unknown since the rays are generated from the sky. Another difference is that one cannot arbitrarily introduce more rays from the surface, as the rays in the occlusion imaging technique represent true visibility from the sky to a ground-based location. The proposed occlusion approach requires significant overlap between flight strips for the surface points to be visible from multiple sky locations.

Figure 9 shows an example where entire flight strips were used as sky locations. These flight strips were acquired using the flight path geometry explained in Section 2.1, which enabled having an overlap of at least 67% between adjacent strips. Figure 9a shows a single flight strip, and Figure 9b-9d show the cumulative addition of a second, third, and fourth strip respectively. Because the upper, leftmost portion of Figure 9a is covered only by the original, single flight strip, its visibility remains lower than the others. In contrast, the first flight strip's middle third is covered by the leftmost third of the second strip. Its rightmost third (bottom right portion) is covered by three portions of three strips: (1) the middle third of the second strip, (2) the leftmost third of the third strip, and (3) a small amount of the fourth strip. In the final data set, the upper leftmost portion of the original strip gains additional coverage points when the flight strips are collected perpendicularly, as shown schematically in Figure 2b. A traditional flight path would typically have a specific point covered by a minimum of one flight track and a maximum of two. The proposed technique seems to work well when there is coverage from six flight tracks, as was done in this work.

5. Results and Discussion

In the previous section, the fundamental principles of ambient occlusion were presented, along with a novel imaging technique that employed these ideas for visualisation of urban ALS data. This section first explains computational aspects of the proposed occlusion imaging method, and then presents the output images created with this technique by investigating the effects of the different parameters and by comparing them with the predominant imaging technique of elevation imaging. The ALS colour and intensity images presented previously (Section 4, Figure 3a and Figure 3b) were not considered here since they were not found to be individually well-suited for visualisation of urban ALS data due to the complexity and high level of detail in urban centres.

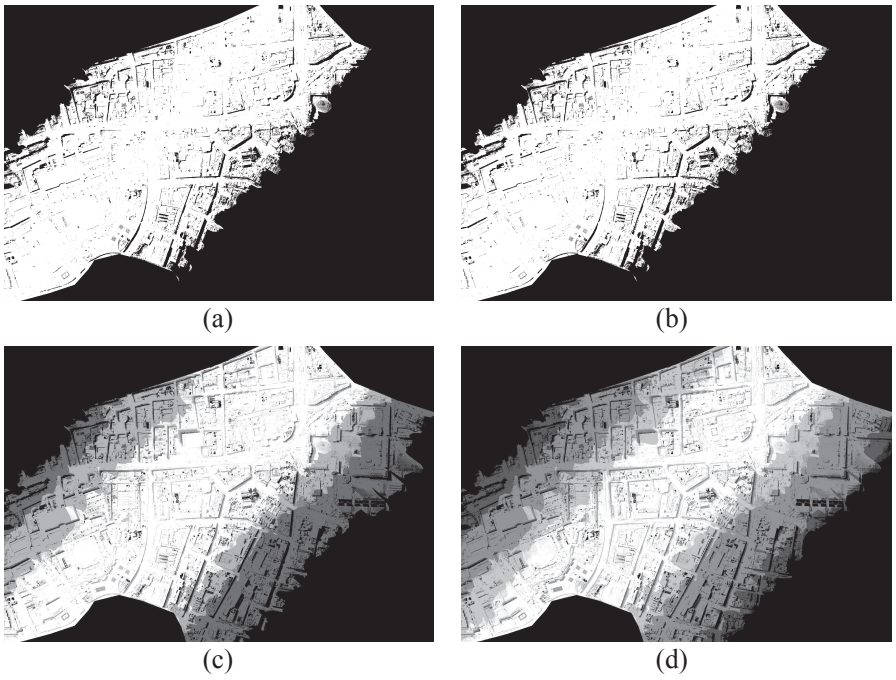

Figure 9: Visibility accumulation for: (a) one flight strip, (b) two flight strips, (c) three flight strips, and (d) four flight strips. In each case, total visibility was normalised to the range $[0, 1]$. Pixel dimensions are $\Delta x = \Delta y = 0.50\ m$.

5.1. Computational Aspects

There were 40 flight strips comprising a total of $\sim 5.4\ GB$ of data. As each flight strip was stored in a separate file, there was one LAS file per strip. The authors developed a program in C++, which read one flight strip at a time, irrespective of whether elevation or occlusion images were the intended output. In all cases, the peak memory consumption was $\sim 1.1\ GB$. This is entirely based on how the data were divided on the disk. In this case, it was one file per flight strip. Table 2 shows the run-times of the program for generating elevation and occlusion images with pixel dimensions in global coordinates: $\Delta x = \Delta y = 0.50\ m$. Notably, no attempt to optimize the implementation was made. Such optimization could be easily implemented on a GPU, in which case the application becomes almost entirely I/O limited.

Table 2: Comparison between the processing times of generating elevation and occlusion images. For all images, pixel dimensions in global coordinates are: $\Delta x = \Delta y = 0.50\ m$

Items	Elevation Image	Occlusion Image	Occlusion Image	Occlusion Image
Nr. of Flight Strips	40	40	40	40
Memory Consumption (GB)	1.1	1.1	1.1	1.1
Processor Specification	Intel Core i7 CPU @ $2GHz$			
Sampling Level	Flight Track	Flight Track	Flight Segment	Scan Line
Execution Time (s)	146.4	116.4	156.4	4894.5

5.2. Varying Flight Path Sampling

As explained in Section 4, different durations of the flight path can be treated as unique sky locations during the creation of occlusion images. Figure 10 shows three different occlusion images of the same area with pixel dimensions in global coordinates: $\Delta x = \Delta y = 0.50\ m$. In Figure 10a, the flight path was sampled at the scan line level. Because a large number of unique sky locations were considered, the contrast in this image is very high. In Figure 10b every flight path segment (1 second) was treated as a unique sky location. The amount of detail visible in this image is similar to the one on the left, albeit at a slightly lower contrast. In Figure 10c, where entire flight tracks were treated as unique sky locations, the outcome blurs small features. While this blurring produces a smoother image and effectively removes vegetation, it does so at the cost of hiding buildings details.

In summary, the choice of flight path sampling affects the balance between contrast, detail, and smoothness. Using a larger number of unique sky locations provides the best contrast and detail, while making the imaging process more sensitive to variations in aircraft orientation. On the other hand, using fewer unique sky locations reduces contrast and visibility of small details but produces smoother images.

5.3. Varying Pixel Dimensions

Besides flight path sampling, pixel dimensions are an important parameter in occlusion images. The three images shown in Figure 11 show the same area visualised at different pixel resolutions. In all three images sky locations were sampled at the flight path segment level. Figure 11a is a high-resolution occlusion image with pixel dimensions $\Delta x = \Delta y = 0.20\ m$ in global coordinates. The small size of the pixels in this image prevents visibility from

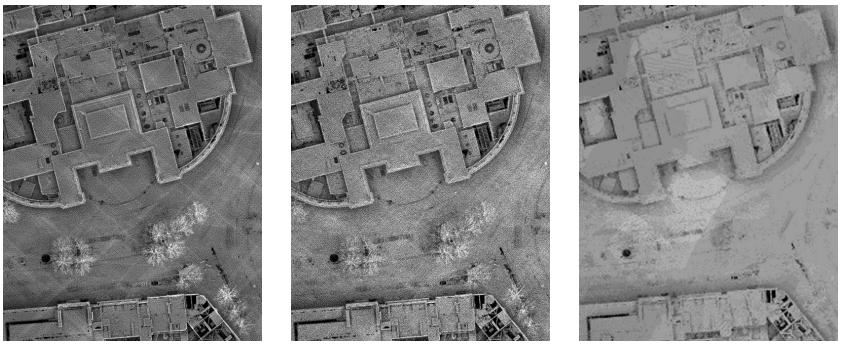

Figure 10: Three different occlusion images of the same area created with different flight path sampling: (a) Scan line sampling. (b) Flight segment sampling. (c) Flight track sampling. Pixel dimensions are: $\Delta x = \Delta y = 0.50\ m$ in all images.

being distributed evenly among the ALS points, which manifests as graininess in the image. Figure 11b has pixel dimensions $\Delta x = \Delta y = 0.50\ m$ in global coordinates. Using slightly larger pixels eliminates much of the graininess, but the increased pixel size makes identifying small features such as details on roofs slight more difficult. Figure 11c has pixel dimensions $\Delta x = \Delta y = 1.0\ m$ in global coordinates. Again, increasing the pixel dimensions produces an even smoother image but at the price of further reduced amount of detail in the image.

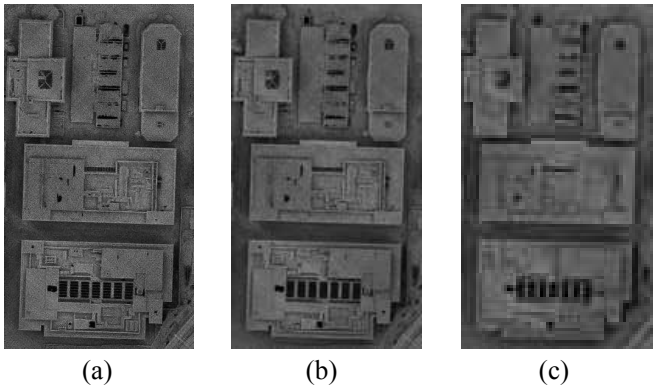

Figure 11: Three occlusion images of the same area sampled at flight path segment level with varying pixel dimensions. (a) $\Delta x = \Delta y = 0.20\ m$. (b) $\Delta x = \Delta y = 0.50\ m$. (c) $\Delta x = \Delta y = 1.0\ m$.

5.4. Occlusion Images versus Elevation Images

While the primary advantage of occlusion images is to provide effective visualisation of building boundaries, there are further advantages. Unlike conventional elevation images, occlusion images suppress moving objects such as vehicles. Since the aircraft will normally pass over the same location several minutes apart, most moving objects in the first scan will be absent in the second scan, thereby resulting in lower overall visibility for the object, and effectively removing transient objects from the occlusion image, without any explicit post-processing for object removal. Similarly, where colour and elevation images often fail to give details of roof structures, the occlusion image clearly displays features such as roof ventilators as shown in Figure 12.

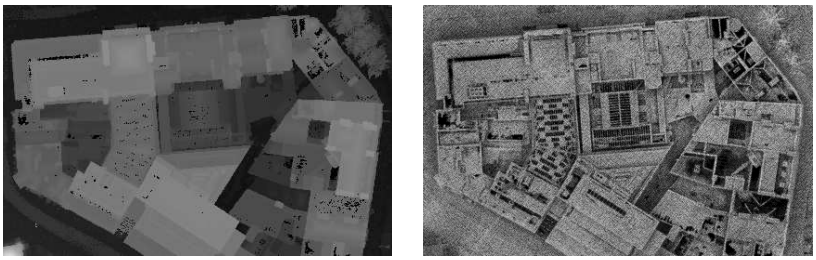

(a) (b)

Figure 12: Comparison between roof detail visualisation in an elevation image (a) and an occlusion image (b). Pixel dimensions are $\Delta x = \Delta y = 0.25\ m$ in both images. Note that neither of these images were contrast enhanced after being cropped out of larger images.

To illustrate the strengths and weaknesses of the occlusion method in the suppression of moving objects and foliage, a section of the data set was selected that contained heavy traffic flow in the form of double decker buses, as shown in Figure 13. In the elevation image (Figure 13a), 56 buses are visible as the long rectangles on the streets. In the occlusion image (Figure 13b), they do not appear. What does, however, appear in the occlusion image are three strings of parked cars (shown with red arrows in Figure 13b). The occlusion technique is less effective in suppressing foliage than with moving object, but still better than the elevation image, as more of the built structures are visible. One example of this is the masonry wall, where the occlusion image shows it as nearly continuous (inset image 1). Another example is in the top right hand corner just above the line of parked cars (inset image 2). The suppression is not intentional only a positive side effect of the technique.

Figure 13: Comparison of suppressing moving objects and foliage: (a) elevation image and (b) occlusion image. In the occlusion image, the process is shown to be able to suppress the visualization of moving cars, in contrast, parked cars still appear (examples shown by the three red arrows). Pixel dimensions are $\Delta x = \Delta y = 0.25\ m$ in all images. The small upper images (shown as 1 and 2 in image (a) are close ups.

The visual clarity of the occlusion images raises the question as to their appropriateness for tasks such as building extraction. To explore this, the Canny method was used in MATLAB for edge detection on both the elevation and occlusion images. Since the occlusion image is a 256 grey-scale levels image, an elevation image with 256 grey-scale levels was used also and not a Digital Surface Model (DSM) containing real height values which is normally the basis for automated analysis. An example of the output is shown in Figure 14 for both an elevation image and an occlusion image. An initial response to these images may be to propose that the elevation-based image is superior for edge detection. However, a closer inspection shows that many key features are lost with the elevation image. Although the occlusion images exhibit noise in the final results, they retain a high level of details as to the changes in the elevations of portions of buildings, the presence of roof features such as fans and penthouses, and the existence of smaller apertures between built features. These types of details can be the controlling factors in micro-climate modelling for wind speed, pollution dispersion, and blast

wave propagation. So within the context of engineering, although the occlusion images do not seem to be directly appropriate for edge detection without the application of additional procedures, they do preserve crucial details that are needed for computational modelling of many important urban topics for which building reconstruction is an integral part. Arguably, performing the edge detection on a DSM instead of the elevation image may deliver more detailed edges since the DSM contains real height values, thereby preserving small height differences.

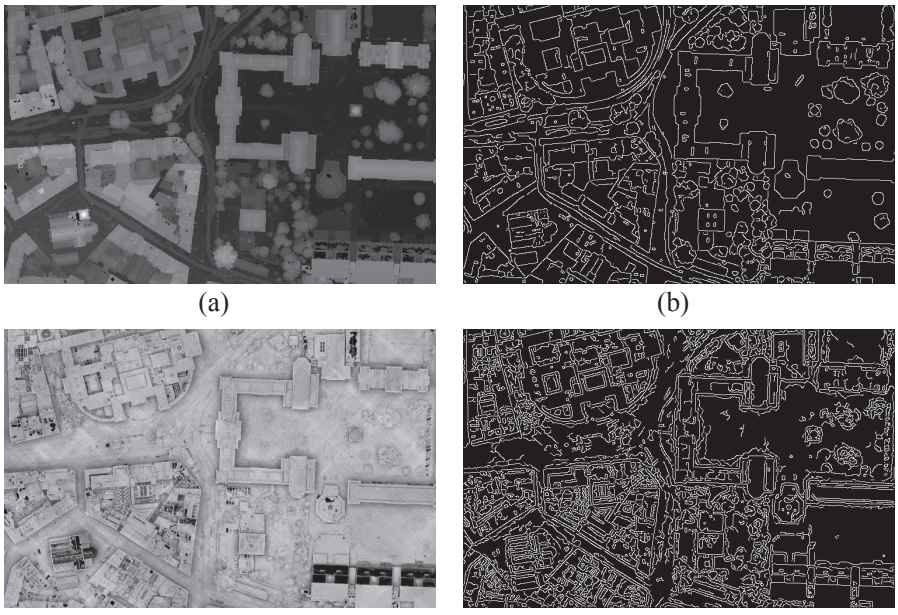

Figure 14: Edge detection comparison: (a) an elevation image; (b) detected edges for the elevation image in part (a); (c) an occlusion image; (d) detected edges for the occlusion image in part (c). Pixel dimensions are $\Delta x = \Delta y = 0.50\ m$.

5.5. Additional Considerations

Figure 15 shows the sensitivity of the technique with respect to the two aforementioned parameters of pixel dimensions and flight component. At specific pixel dimensions, flight segment sampling gives a better final image than either scan line or flight track sampling. However, by reducing the pixel dimensions, an equivalent image can be achieved with the flight track sampling. This is most easily seen by comparing the flight segment sampling

at the $\Delta x = \Delta y = 0.50\ m$ pixel dimensions to the flight track sampling at the $\Delta x = \Delta y = 0.25\ m$ m pixel dimensions. Selection of such parameters will require the application of the technique to a wide range of data sets before optimization advice can be given.

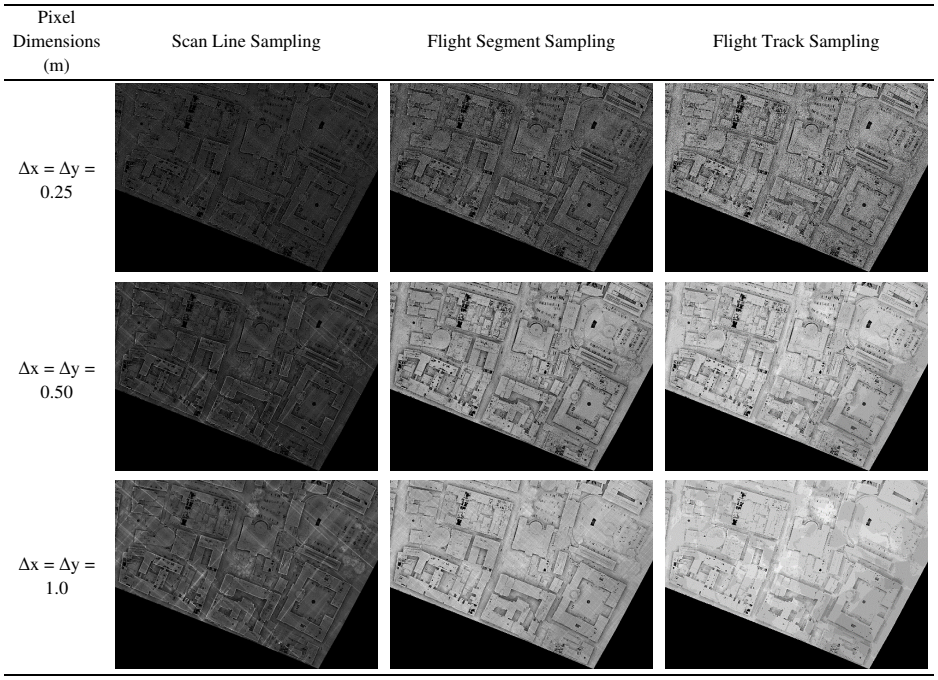

Figure 15: Comparison of occlusion images generated with different pixel dimensions and different definitions of sky location.

Trying to adapt this technique for terrestrially ground-based laser scanning (either stationary Terestrial Laser Scanning (TLS) or Mobile Laser Scanning (MLS)) would require modifications in the data capture approaches currently adopted. Specifically, TLS has small amount of overlap between scans. Unless the data caprure approach was changed by scanning the study area from several locations, the proposed occlusion method would have little value to the processing of that data. Furthermore, in case of scanning a tall multi story building, TLS generates a lot of occlusions for window areas (especially the recesses) on upper floors, as well as the roofs. If this could be overcome by placing a terrestrial unit on the roof of the highest building in the study area, many of the occluded areas could be made visible. However, this is not currently standard practice.

6. Conclusions and Future Work

Dense urban ALS data pose particular challenges to visualisation and building identification, due to the complexity of urban centres and the existence of foliage and moving objects. This paper introduced the concept of occlusion images as a means to improve visualization of ALS datasets. The idea is based on an inversion of the ambient occlusion approach. Furthermore, this paper demonstrated that occlusion images suppress moving objects and to lesser degree foliage, thus simplifying building identification and extraction, if those steps are desired.

The technique presented in this paper exclusively uses the ALS data and restricts itself to the occlusion image approach. However, for dense urban areas, combining this method with conventional ALS visualisation techniques and even other data sets may give more complete information depending upon the goal of the visualisation and the characteristics of the local building stock.

In the future, the occlusion technique can be extended to handle full waveform ALS data (e.g. (Persson et al., 2005; Mallet et al., 2011)), thereby enabling pulse visibility mapping to be applied beyond the information available in the discrete echoes that were used herein.

7. Acknowledgments

This work was generously supported by Ireland's Science Foundation grant 05/PICA/I830, Ireland's Environmental Protection Agency grant 2005-CD-U1-M1, and by the European Union's ERC-2012-StG-20111012 Project 307836. Thanks are also due to Fugro and BKS for accommodating the non-standard scan requirements.

References

Arnold, N.S., Rees, W.G., Devereux, B.J., Amable, G.S., 2006. Evaluating the potential of high-resolution airborne lidar data in glaciology. International Journal of Remote Sensing 27 (5-6), 1233–1251.

Awrangjeb, M., Ravanbaksh, M., Fraser, C., 2010. Automatic detection of residential buildings using lidar data and multispectral imagery. ISPRS Journal of Photogrammetry and Remote Sensing 65 (5), 457–467.

Baltsavias, E.P., 1999a. Airborne laser scanning - an introduction and overview. ISPRS Journal of Photogrammetry & Remote Sensing 54 (2-3), 68–82.

Baltsavias, E.P., 1999b. Airborne laser scanning: basic relations and formulas. ISPRS Journal of Photogrammetry & Remote Sensing 54 (2-3), 199–214.

Baltsavias, E.P., 1999c. Airborne laser scanning: existing systems and firms and other resources. ISPRS Journal of Photogrammetry & Remote Sensing 54 (2-3), 164–198.

Baltsavias, E.P., 1999d. A comparison between photogrammetry and laser scanning. ISPRS Journal of Photogrammetry & Remote Sensing 54 (2-3), 83–94.

Clode, S., Rottensteiner, F., 2007. Detection and vectorization of roads from lidar data. Photogramm. Eng. Remote Sens. 73 (5), 517–536.

Corbane, C., Saito, K., Dell'Oro, L., Gill, S.P.D., Piard, B.E., Huyck, C.K., Kemper, T., Lemoine, G., Spence, R.J.S., Shankar, R., Senegas, O., Ghesquiere, F., Lallemant, D., Evans, G.B., Toro, R.A.G.J., Ghosh, S., Svekla, W.D., Adams, B.J., Eguch, R.T., 2011. A comprehensive analysis of building damage in the 12 January 2010 MW7 Haiti earthquake using high resolution satellite and aerial imagery. Photogrammetric Engineering & Remote Sensing 77 (10), 997–1009.

Dorninger, P., Pfeifer, N., 2008. A comprehensive automated 3d approach for building extraction, reconstruction, and regularization from airborne laser scanning point clouds. Sensors 8, 7323–7343.

Elberink, S.O., 2010. Acquisition of 3D topography - Automated 3D road and building reconstruction using airborne laser scanner data. Ph.D. thesis. University of Twente.

Geist, T., Lutz, E., Stötter, J., 2003. Airborne laser scanning technology and its potential for applications in glaciology. International Archives of Photogrammetry, Remote Sensing & Spatial Information Sciences 34 (3/W13), 101–106.

Haala, N., Brenner, C., Anders, K.H., 1998. 3d urban gis from laser altimetry and 2d map data. International Archives of Photogrammetry & Remote Sensing 32 (3), 339–346.

Hinks, T., Carr, H., Laefer, D.F., 2009. Flight optimization algorithms for aerial lidar capture for urban infrastructure model generation. Journal of Computing in Civil Engineering 23 (5), 330–339.

Hofle, B., 2007. Detection and Utilization of the Information Potential of Airborne Laser Scanning Point Cloud and Intensity Data by Developing a Management and Analysis System. Ph.D. thesis. University of Innsbruck.

Hollaus, M., Wagner, W., Eberhöfer, C., Karel, W., 2006. Accuracy of large-scale canopy heights derived from lidar data under operational constraints in a complex alpine environment. ISPRS Journal of Photogrammetry & Remote Sensing 6 (5), 323–338.

Hollaus, M., Wagner, W., Kraus, K., 2005. Airborne laser scanning and usefulness for hydrological models. Advances in Geosciences 5, 57–63.

Huang, H., Brenner, C., Sester, M., 2013. A generative statistical approach to automatic 3d building roof reconstruction from laser scanning data. ISPRS Journal of Photogrammetry and Remote Sensing 79, 29–43.

Jensen, H.W., 2009. Realistic Image Synthesis Using Photon Mapping. A. K. Peters, Ltd., Natick, MA, USA.

Laefer, D.F., Pradhan, A., 2006. Evacuation route selection based on tree-based hazards using lidar & gis. Journal of Transportation Engineering 132 (4), 312–320.

Langer, M.S., Buelthoff, H.H., 2000. Depth discrimination from shading under diffuse lighting. Perception 29 (6), 649–660.

Latypov, D., 2005. Effects of laser beam alignment tolerance on lidar accuracy. ISPRS Journal of Photogrammetry & Remote Sensing 59 (6), 361–368.

Mallet, C., Bretar, F., Roux, M., Soergel, U., Heipke, C., 2011. Relevance assessment of full-waveform lidar data for urban area classification. ISPRS Journal of Photogrammetry and Remote Sensing 66 (6), S71–S84.

Matikainen, L., Kaartinen, H., Hyyppä, J., 2007. Classification tree based building detection from laser scanner and aerial image data. International Archives of Photogrammetry, Remote Sensing & Spatial Information Sciences 3 (3/W52), 280–287.

Melzer, T., Briese, C., 2004. Extraction and modeling of power lines from als point clouds, in: Proceedings of 28^{th} Workshop of the Austrian Association for Pattern Recognition (ÖAGM), pp. 47–54.

Persson, A., Söderman, U., Töpel, J., Ahlberg, S., 2005. Visualization and analysis of full-waveform airborne laser scanner data. International Archives of Photogrammetry, Remote Sensing & Spatial Information Sciences 36 (3/W19), 103–108.

Rottensteiner, F., Trinder, J., Clode, S., Kubik, K., 2005. Using the dempstershafer method for the fusion of lidar data and multi-spectral images for building detection. Information Fusion 6 (4), 283–300.

Rutzinger, M., Höfle, B., Hollaus, M., Pfeifer, N., 2008. Object-based point cloud analysis of full waveform airborne laser scanning data for urban vegetation classification. Sensors 8, 4505–4528.

Stewart, A.J., Langer, M.S., 1997. Towards accurate recovery of shape from shading under diffuse lighting. IEEE Transactions on Pattern Analysis and Machine Intelligence 19, 1020–1025.

Tournaire, O., Brédif, M., Boldo, D., Durupt, M., 2010. An efficient stochastic approach for building footprint extraction from digital elevation models. ISPRS Journal of Photogrammetry and Remote Sensing 65 (4), 317–327.

Yu, X., Hyyppä, J., Vastaranta, M., Holopainen, M., Viitala, R., 2011. Predicting individual tree attributes from airborne laser point clouds based on the random forests technique. ISPRS Journal of Photogrammetry and Remote Sensing 66 (1), 28–37.

Zhukov, S., Inoes, A., Kronin, G., 1998. An ambient light illumination model, in: Drettakis, G., Max, N. (Eds.), Rendering Techniques '98, Springer-Verlag, Wien, New York. pp. 45–56.